Doped TiO_2-Ge Nanocomposites for Thermoelectric Applications

by

R. Andrew Hackendorn

A thesis submitted to the Faculty of the University of Delaware in partial fulfillment of the requirements for the degree of Bachelor of Science in Mechanical Engineering with Distinction.

Spring 2010

Copyright 2010 Hackendorn

All Rights Reserved

Doped TiO_2-Ge Nanocomposites for Thermoelectric Applications

by

R. Andrew Hackendorn

Approved: _____

S. Ismat Shah, Ph.D.

Professor in charge of thesis on behalf of the Advisory Committee

Approved: _____

Ajay Prasad, Ph.D.

Committee member from the Department of Mechanical Engineering

Approved: _____

Victor Kaliakin, Ph.D.

Committee member from the Board of Senior Thesis Readers

Approved: _____

S. Ismat Shah, Ph.D.

Chair of the University Committee on Student and Faculty Honors

ACKNOWLEDGMENTS

The journey through this research endeavor has been greatly fulfilling, yet would not have been possible without several people. First and foremost, I would like to thank my parents and family for giving me the opportunity to enjoy the life I have been blessed with. They have respected and appreciated all the hard work that goes into being an engineering student. Next, I would like to thank everyone in the lab, especially Dr. Shah for giving me the chance to work in his lab and being both a friend and teacher, Emre, who has worked with me since day one, and without him this thesis would have been impossible, Hassnain, who has been a great friend and mentor, and has truly set the level for work ethic, and everyone else I have met over the last years. Lastly, I would like to thank all of my closest friends for being by my side through the bad times and the good times.

TABLE OF CONTENTS

LIST OF TABLES

LIST OF FIGURES

ABSTRACT

Titanium dioxide has shown promise as the basis for a thermoelectric material as it is an excellent thermal insulator and is able to be alloyed, in this case with germanium, to enhance electrical properties. In general, this thermoelectric material will produce an electrical potential when there exists a temperature gradient across the material. As such, it is important for the material to have a high electrical conductivity and a low thermal conductivity, creating a conflict since these properties naturally increase or decrease simultaneously. RF sputtering has shown to be an efficient way of synthesizing TiO_2-Ge thin films in such a way that the electrical properties are enhanced while minimally altering the thermal properties as compared to bulk TiO_2. Films were deposited onto quartz substrates for two hours and heated to 600^{o}C with RF power of 200W sent through the magnetron sputtering gun. Films at three different pressures, 5mtorr, 10mtorr, and 15mtorr were deposited with target TiO_2:Ge:Sb compositions of 55:45:0, 30:70:0 and 54:45:1. The final composition introduced antimony as a dopant to enhance the electrical conductivity. Significant increases in the electrical conductivity was seen in the films as compared to bulk TiO_2, and a slight increase was seen between the undoped to doped samples. The Seebeck measurements for each sample offered a positive trend in measurements up to 200^{o}C, which is promising for higher temperature applications. Lastly, the amorphization of TiO_2 can be seen while maintaining Ge crystallinity, which is promising for obtaining low thermal conductivity.

Chapter 1

INTRODUCTION

Recent economic instabilities and growing environmental concerns have brought about widespread research in the fields of clean energy generation and energy harvesting. As the price of fossil fuels steadily increase, most notably crude oil peaking at over $140 per barrel last year [1], it is of utmost importance to increase the efficiency of devices which will ultimately aid in decreasing the dependence on fossil fuels. Of the many methods being explored, thermoelectric devices serve as a very promising route to increase device efficiencies by converting waste heat into usable electricity. Conversely, the same device can generate thermal energy if it is supplied an electrical source. Furthermore, these devices enjoy very long lifetimes as there are no moving parts nor are there any materials consumed during the conversion process. An industrial leader in the production of thermoelectric devices claimed over 100,000 hours of steady state operation possible without any maintenance [2]. As research rapidly progresses, and the demand for cleaner and more efficient energy increases, thermoelectrics show a promising outlook for the years to come.

As people live their everyday lives, the severity with which energy is wasted is often overlooked. While it is generally seen that the consumers contribute most to the waste, it is in fact the devices themselves operating at low efficiencies which squander useful energy. Perhaps the best example of a system with high thermal energy losses is the internal combustion engine of a standard vehicle. As reported by the United States Department of Energy, the standard internal combustion engine loses 62.4% of the initial

energy of the gasoline as a direct result of friction and heat losses [3]. This accounts for the largest source of energy loss within a standard vehicle, and when combined with various other losses, leads to an overall utilization of only 15% of the initial energy potential of the fuel [3][4]. With an optimized thermoelectric device, a portion of the heat that is currently vented to the environment could be converted into electricity. The electricity could then be used to supplement various components of the vehicle. It is applications like this that are needed to increase efficiency of energy usage that could drastically reduce the dependence on fossil fuels.

1.1 Main Process

All thermoelectric materials and devices rely on the Seebeck effect, first introduced by Thomas Johann Seebeck, which is the direct conversion of a temperature differences across a material into electric voltage, and vice versa. The thermoelectric effect arises when charge carriers become free to move and in doing so, carry the charge, as well as heat. When a temperature gradient is applied to such a material, the mobile charge carriers tend to migrate towards the colder side from the hot side. The charge carriers begin to build up at the cold end of the material. As this buildup occurs, it creates a net electrostatic potential, or voltage.

When applying the thermoelectric effect to a device, it is often the case that n-type and p-type materials are coupled together. When doing this, and as Figure 1 shows below, the device is often wired electrically in series and thermally in parallel. Notice the electron flow is in the same direction as the heat flow in Figure 2, which would be exactly opposite should the material be p-type [5]. For such a device, it is the temperature gradient and Seebeck effect that provides the voltage ($V=\alpha\Delta T$) and the flow of the heat that drives the electric current, from which a power output is derived.

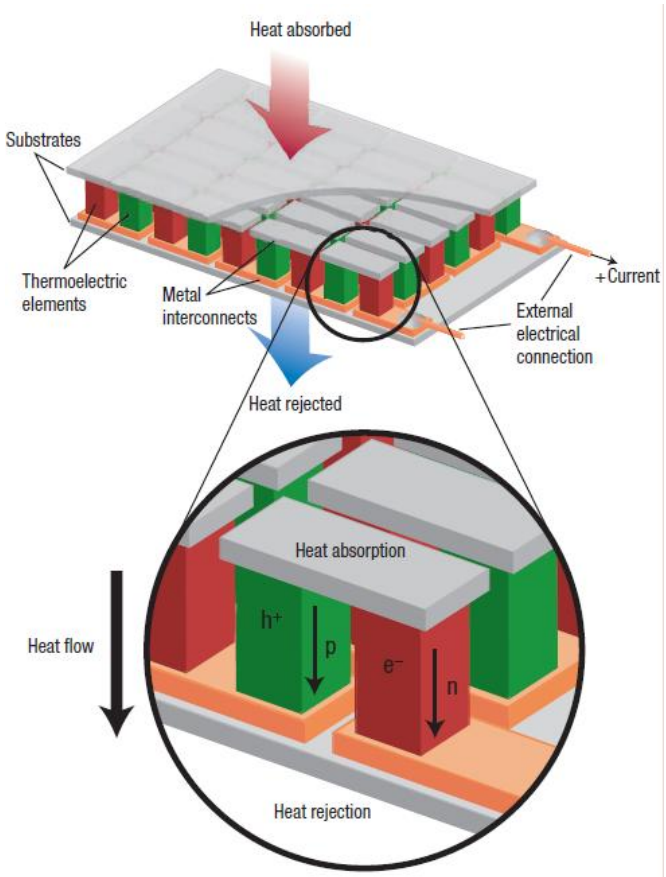

Figure 1 - Thermoelectric Device [6]

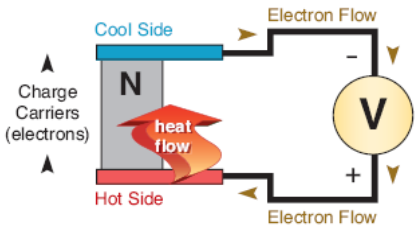

Figure 2 – n-type device [5]

When engineering thermoelectric materials, it is often best to begin with a crystalline semiconductor material that has been heavily doped so as to have transport properties similar to that of a metal. When dopants are introduced, electrons and holes become present within the structure, which in either scenario results in enhanced electrical conductivity. In order to evaluate a thermoelectric material, a figure of merit, *z*T, has been established:

$$zT = \frac{\sigma S^2}{\kappa} \qquad 1.1$$

The figure of merit is based on electrical conductivity (σ), Seebeck coefficient (S), and thermal conductivity (κ).

1.2 Theoretical Background

The field of thermoelectrics requires that several conflicting material properties be optimized. As seen in equation 1.1, to maximize the figure of merit it is necessary to increase both the Seebeck coefficient and electrical conductivity while decreasing thermal conductivity. Since electrical and thermal properties are interrelated, several material characteristics need to be optimized in order to maximize the zT value.

Before continuing, it is important to first understand, in general, how conduction occurs within a semiconductor. As ordered atoms within a crystalline material come into close proximity with each other, electrons are perturbed by the electrons and nuclei of adjacent atoms. This behavior causes the material to have closely spaced electron states, known as electron energy bands [7]. Of the numerous potential energy bands, some are completely filled, partially filled, or not occupied at all. The energy corresponding to the highest filled state, at absolute zero (0K), is known as the fermi energy, E_f.

The final two bands of a material, the valence and conduction bands, are related. The valence band is completely filled with electrons and is separated from the conduction band, which is empty, by an energy band gap. In semiconductors, for an electron to become free it must be promoted from the valence band across the band gap and into the bottom of the conduction band. To do this, the electron must be supplied with the amount of energy difference between the conduction and valence band, known as the band gap energy, E_g.

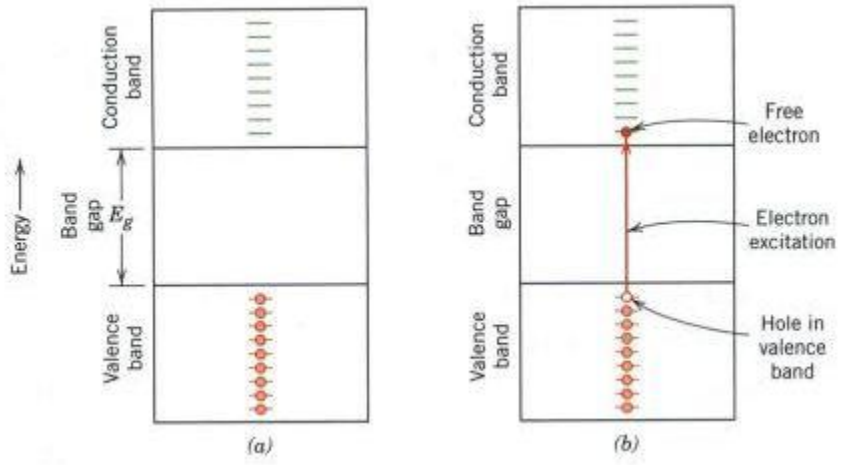

Figure 3 - Before and after electron excitation from the valence band to the conduction band creating both holes and free electrons [8]

As mentioned previously, the charge carrier of a thermoelectric material could be n-type, p-type or some of both. In order to make certain that the Seebeck coefficient is maximized, the type of charge carrier within the material ideally should be limited to either n-type or p-type, but not both. If, for example, the charge carrier type was mixed, there would be a movement towards the cooler side of the material by both types, which would lead to them cancelling each other to some degree. This relationship

can be seen in equation 1.2a, where α and σ are the Seebeck coefficient and electrical conductivity, respectively.

$$\alpha = \frac{\sigma_n \alpha_n + \sigma_p \alpha_p}{\sigma_n \sigma_p} \qquad 1.2a$$

While semiconductors often have relatively large Seebeck coefficients, they also tend to have low carrier concentration. With inherently low carrier concentration, the result is lower electrical conductivity. For a metal or heavily doped degenerate semiconductor, the Seebeck coefficient is given by:

$$\alpha = \left[\frac{8\pi^2 k_B^2}{3eh^2} m^*\right] T \left(\frac{\pi}{3n}\right)^{\frac{2}{3}} \qquad 1.2b$$

where *n* represents the carrier concentration, *m** represents the effective mass of the carrier, k_B is the Boltzmann constant, and *h* is the [6]. Furthermore, the electrical conductivity is related to *n* by:

$$\sigma = ne\mu \qquad 1.3a$$

where μ is the carrier mobility, and *e* is the charge [7]. However, since semiconductors can have two types of charge carriers, holes and electrons, the electrical conduction equation must account for both as shown in equation 1.3b as

$$\sigma = n|e|\mu_e + p|e|\mu_h \qquad 1.3b$$

where μ_e and μ_h represent the mobility of electrons and holes, respectively, while *n* and *p* represent the concentration of electrons and holes, respectively [7]. In an intrinsic semiconductor, the conductivity is not dependant on impurities. Holes are produced only by promoted electrons across the bandgap, thus *n* = *p* and $\sigma = 2n|e|(\mu_e + \mu_h)$. However, in real world applications the extrinsic properties must be used. In an extrinsic

material, the concentration of holes and electrons is different, and the material is classified as n-type when $n>p$, and vice versa. The distribution of concentration between holes and electrons can be described by,

$$n_o p_o = n_i^2 \qquad 1.4$$

where n_o and p_o represent the concentrations of electrons and holes, respectively, and n_i is the intrinsic carrier concentration.

As can be seen from equations 1.2(b) and 1.3(a)(b), as the carrier concentration increases, the Seebeck coefficient decreases while the electrical conductivity increases. This compromise between Seebeck coefficient and electrical conductivity is nicely illustrated in figure 4. The graph also shows an optimized carrier concentration so as to provide the highest thermopower ($\alpha^2\sigma$) which occurs between roughly 10^{19} and 10^{21} charge carriers per cm^3. With this range of carrier concentrations falling between metals and semiconductors, the thermoelectric material with optimal carrier concentration lends itself to heavily doped semiconductors.

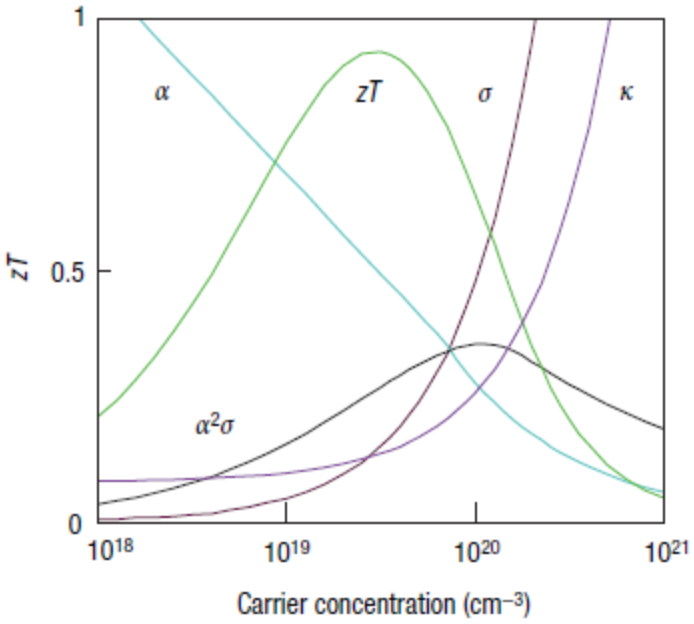

Figure 2 - ZT versus Carrier Concentration[6]

Additionally, the carrier concentration of a semiconductor is dependent on temperature. Intrinsically, concentrations of both holes and electrons drastically increase with temperature due to the increased thermal energy exciting electrons to the conduction band [7]. Extrinsically, the behavior is often very different. At very low temperatures (approaching 0K), for example in *n*-type silicon, there is not enough thermal energy to promote an electron to the conduction band from the valence band. At midrange temperatures, say up to around 450K, the extrinsic electron concentration is roughly constant, and at exceeding temperatures the concentration approaches the intrinsic value [7].

Another conflict in maximizing the figure of merit is found in the thermal conductivity. Within thermoelectric, thermal conductivity can be attributed to two mechanisms, with the first being holes and electrons transporting heat (κ_e), and the

second being phonon motion within the lattice (κ_l). This can be explained by the following equations:

$$\kappa = \kappa_e + \kappa_l \quad (1.5)$$

$$\kappa_e = \sigma LT = ne\mu LT \quad (1.6)$$

where L is the Lorenz factor and for free electrons is equal to $L = 2.4 \times 10^{-8}\ J^2K^{-2}C^{-2}$. However, the Lorenz factor can fluctuate depending on carrier concentration. Typically, in order to determine κ_l, the electrical conductivity (σ) is experimentally found which is then used to take the difference between κ and κ_e. As equation 1.6 shows, the κ_e term is directly proportional to electrical conductivity.

Further development within the field of thermoelectrics aims at creating a material that exhibits low lattice thermal conductivities while maintaining electrical conductivity. Materials like glass have incredibly low lattice thermal conductivity due to the randomness of energy maneuvering throughout the material, unlike the rapid phonon transport of higher thermal conductivity materials. However, glassy materials do not possess the same electrical properties that a crystalline semiconductor does. In glass, high electron scattering and low effective masses causes low electron mobility further leading to inadequate electrical conductivity. Ideally, a thermoelectric material should be able to effectively scatter phonons while minimally disturbing the electrical conductivity. Such phonon scattering mechanisms would carry the heat flow at a variety of wavelengths and mean free paths.

The required set of properties that a thermoelectric material should have is termed a phonon-glass electron-crystal. As described previously, the phonon-glass portion of the material is responsible for minimizing lattice thermal conductivity. The electron-crystal is related to the maximization of electrical properties through the use of crystalline semiconductors. The ability to engineer such a material would optimize the thermal and electrical properties needed for a successful thermoelectric film.

METHODS

2.1 Radio Frequency Magnetron Sputtering Deposition

2.1.1 Background

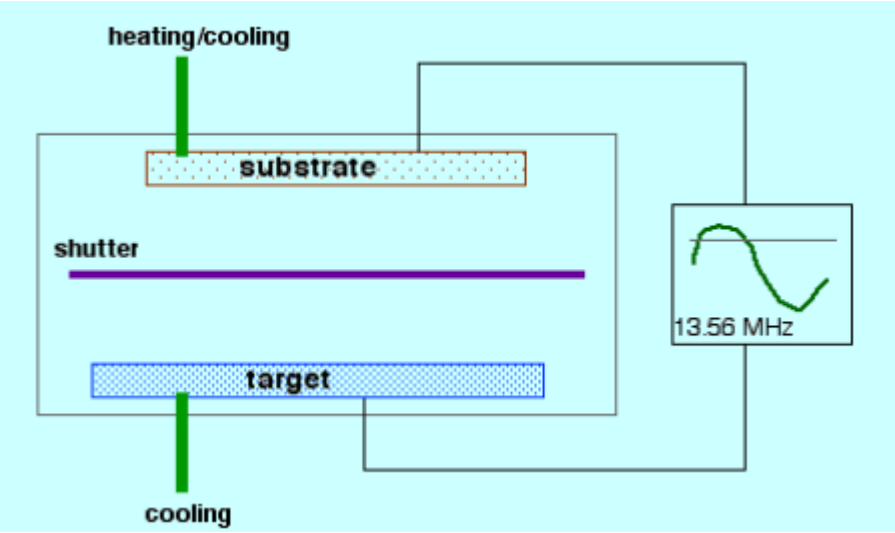

Figure 3 - RF Sputtering Diagram [6]

The material of interest is grown as a thin-film using a physical vapor deposition technique called radio frequency magnetron sputtering. In general, sputtering is a method that ejects the target material from a bulk source and deposits it onto a substrate, such as quartz or silicon. Sputtering occurs under vacuum and relies on the presence of an inert gas, typically argon. The substrate/vacuum chamber and the target act as the anode and the cathode, and due to the radio frequency of the potential, alternate. As inherent electrons within the vacuum chamber are attracted to the anode, they collide with the inert gas knocking out an electron and causing the argon to become

an ionized Ar^+. This process also introduces more electrons to the system, allowing for increased ionization of the argon gas.

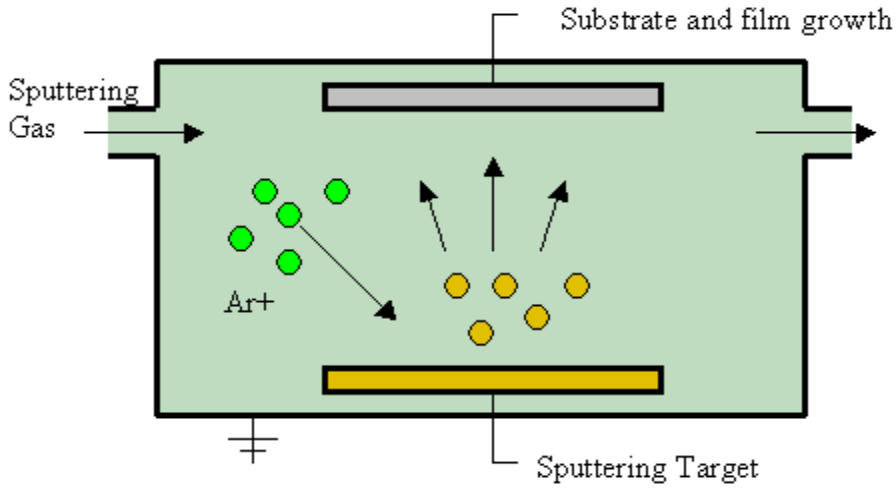

Figure 4 - Physical process of sputtering [9]

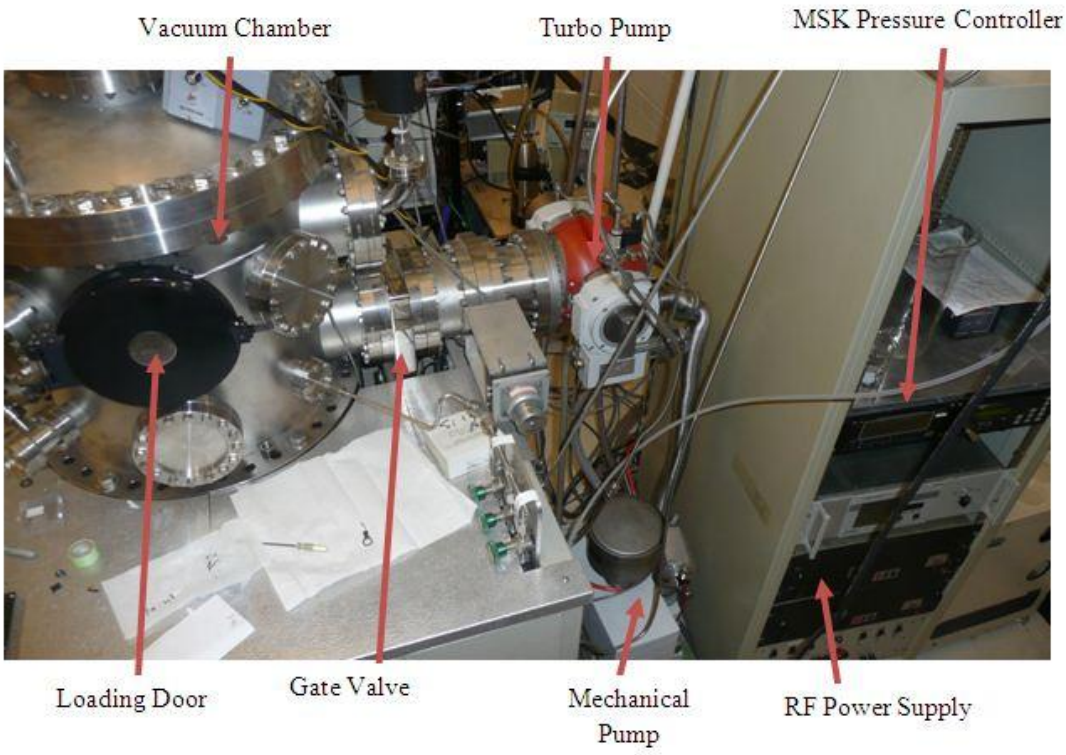

Figure 5 - Sputtering system used for creating films analyzed within this report

Up to this point, no deposition has occurred, however when the target is acting as the cathode, the positively charged argon ions bombard the target surface. As the argon ions bombard the target material, atoms from the target are knocked out and become mobile within the chamber. The atoms from the target material deposit on nearly all surfaces within the chamber but have a cosine distribution with most of the flux going orthogonal to the target surface. Positioning of the substrate correctly, facing the target, allows for sufficient film growth. The reason for using radio frequency sputtering is to avoid charge buildup on the semiconducting target material. For example, in DC sputtering, the target is the cathode and has the tendency for positive charge to quickly collect. By using an alternating potential, this scenario does not occur. Due to these

reasons it is typically the practice to use radio frequency sputtering to deposit insulating or semiconducting oxide films.

While the above mentioned deposition of the target material occurs when the target acts as the cathode, due to radio frequency the substrate also acts as the cathode sometimes. However, the substrate and the entire vacuum chamber are electrically connected, so the entire system (except the target) acts as the anode and cathode throughout the cycles. The large area minimizes the sputtering of the substrate. If, for example, the substrate was the entire cathode, the newly deposited film would be sputtered away.

As mentioned, the system used is also a magnetron sputtering system, meaning that a substantial magnetic field is introduced directly behind the target. The goal of this is to increase the ionization of the argon which will further increase the sputtering rates. When the magnet is introduced, it traps more electrons near the target surface, causing a higher probability of electron collisions with the argon neutrals. As more of these collisions happen, more argon atoms become ionized and due to the close proximity to the target, cause increased Ar^+ bombardment of the target material.

2.2 Experimental Setup

As previously described, the standard choice for thin-film growth of insulating materials is RF magnetron sputtering. Shown above in Figure 7 are schematics for the particular sputtering device used. While the chamber is at standard temperature and pressure the substrate and target material is loaded into the system. The targets were formed by mixing the desired weight percent of pure TiO_2 powder (99.999%, Degussa Aeroxide) and pure germanium powder (99.999%, 100 mesh, Sigma Aldrich). For the

later trials, pure antimony was also added. Using a mortar and pestle, the base materials were thoroughly mixed for roughly 2 hours. The mixed TiO_2-Ge was compacted into 2" copper cups to a thickness of ¼". To harden the target so that it does not disintegrate upon sputtering, the targets are inserted into a hydraulic press and compacted under 50,000 psi for roughly 2 hours. Targets were made with TiO_2:Ge ratios of 45:55 and 70:30. Also, for antimony doped trials, targets with TiO_2:Ge:Sb ratios of 64:33:3 and 54:45:1 were made.

The substrates that the films were grown on were SiO_2 (quartz glass) cut to ½" x ½" squares, as well as 1½" x 3/8" rectangles. The squares are sized for the majority of the film characterization techniques, except for Seebeck measurements. For the Seebeck measurements, it is better to have films with higher length to width ratio which is the reason for the longer, rectangular substrates. The substrate holder and heater allow for a single rectangular substrate and up to three square substrates during a single deposition. For these trials, a single rectangle and two square substrates were used for each concentration.

Following the installation of the target and substrates, the chamber was evacuated using a mechanical pump and Pfeiffer Balzers TPG 510 turbo pump in series. The pumping system was allowed to reach a base pressure of $5x10^{-6}$ torr as measured by an ion gauge. After reaching this base pressure, the substrates were heated using a variac controlled resistance heater to a temperature of 600^oC. Based on research performed previously in the Shah lab, a deposition temperature of 600^oC has shown to be best for crystalline growth of TiO_2. After allowing the substrates to reach 600^oC pure argon gas was introduced to the system. Depending on the sample being made, the pressure was set to 5mtorr, 10mtorr, or 15mtorr using an MKS 600 pressure controller. The variation in

pressure is aimed at influencing the rate of argon ionization and furthermore the rate of Ar^+ bombardment of the target material.

Prior to each deposition the target was pre-sputtered for roughly 30 minutes at 55W (RF Plasma Products Inc) to remove any oxidation or extraneous materials that may have accumulated on the surface. To minimize the amount of target material depositing on the substrate during pre-sputter, a shutter sits roughly 1cm above the target blocking the plasma. In addition, the substrate holder has a small motor allowing it to rotate 360^o, further allowing the substrates to be moved to the opposite side of the chamber. Deposition then occurred for 2 hours at 200W and 600^oC for all samples, with pressure being the only deposition parameter that changed. To assure sufficient film growth on the substrate, the substrate holder is located roughly 2.5 inches above the target.

After depositing for 2 hours, the power supply is turned off and the argon is allowed to run post deposition for 10 minutes. The argon and heater are then turned off, and the chamber is allowed to cool to room temperature which typically take several hours. After the substrates and chamber have cooled to room temperature, they are removed for characterization and analysis.

2.3 Analysis

2.3.1 X-Ray Diffraction

X-Ray Diffraction (XRD) is a technique that is widely used to analyze the crystal structure, grain size, phase, and plane orientation of samples. Cu K-a radiations (1.5405 A) are aimed at the sample of interest. Upon penetrating the sample the X-ray

radiation diffracts at a unique angle, known as the 2θ angle, depending upon the plane the X-rays are incident on. This is the angle between the beam and the diffraction source. Once the X-Ray radiation diffracts through the sample, a detector collects the radiation and plots the intensity of the collected radiation versus 2θ. The diffraction follows Bragg's formula, $n\lambda = 2\sin\theta$.

The plot obtained from the XRD is used to determine the sample's crystallinity based on the peaks as they compare in intensity to the background noise. Also, phase can be determined by peak position comparing the same data to several tabulated diffraction databases.

In the case of TiO_2-Ge, it is important to control the size of the Ge grains within the lattice structure. The specific grain size of Ge within each sample can be evaluated and computed from the full width at half maximum (FWHM) of the peaks using the Sherrer equation [10]. In general, the sharper the peak, the larger the crystallite size, as shown by the equation:

$$\beta_{hkl} = \frac{K\lambda}{L_{hkl} cos\theta_{hkl}} \qquad 2.1$$

In the above equation β_{hkl} is the line broadening at half the maximum intensity (FWHM) in radians. K is the shape factor which ranges between 0.89 and 1 depending on the breadth method, λ is the incident X-Ray wavelength, L is the crystallite size and θ is the Bragg angle or the angle at the center of a peak.

The system used for analyzing the prepared films is a Rigaku D-Max B diffraction device. The system operates with a Cu (Kα) radiation source of wavelength

λ=1.5405 Å and a graphite crystal monochromator. Survey scans of the samples were conducted from $2\theta = 20^o - 80^o$ with a step size of 0.02^o.

2.3.2 Secondary Electron Microscopy

Scanning electron microscopy (SEM) uses an electron beam to scan the surface of the sample, therefore causing electrons to interact with the target sample. The interaction with the incident electron beam leads to the ionization of the specimen ultimately producing secondary electrons. Using a secondary electron detector, surface topography and surface composition can be imaged. In addition to secondary electrons, it is common for the electrons of the incident beam to directly impact an atom of the sample, which leads to a scatter 180^o backwards. Another type of detector can sense these electrons, providing another method to image a sample. In addition to imaging, the SEM can also determine surface composition of a sample using an ultra-thin window Energy Dispersive X-Ray Spectroscopy (EDAX).

SEM was used for both surface analysis and thickness measurements. In order to measure film thickness, samples were cut in half allowing for a true cross section of the film to be exposed. The reported images within this report came from a JEOL JSM-7400F high resolution scanning electron microscope. The resolution of this model SEM is 1.5nm at 1kV and 1.0nm at 15kV. A working distance between 7mm and 8mm was maintained as well as an accelerating voltage between 2kV and 5kV.

2.3.3 Seebeck Measurements

As described in above theory, the general equation for determining the Seebeck coefficient is given by

$$\alpha = \frac{\Delta V}{\Delta T} \qquad 2.2$$

where ΔV is the thermoelectric voltage across the material and ΔT is the temperature gradient across the material. A device was fabricated to measure the Seebeck coefficient of thin films up to several hundred degrees Celsius. Below is a picture which depicts the Seebeck measurement device. The device houses two high temperature halogen bulbs, separated by a thick ceramic insulator, direct heat upwards towards the sample. The bulbs are controlled individually using two variac voltage controllers. Each end of the sample makes contact with the heated stage only through two 1cm x 1cm aluminum cubes at each end of the sample, in order to assure a temperature gradient.

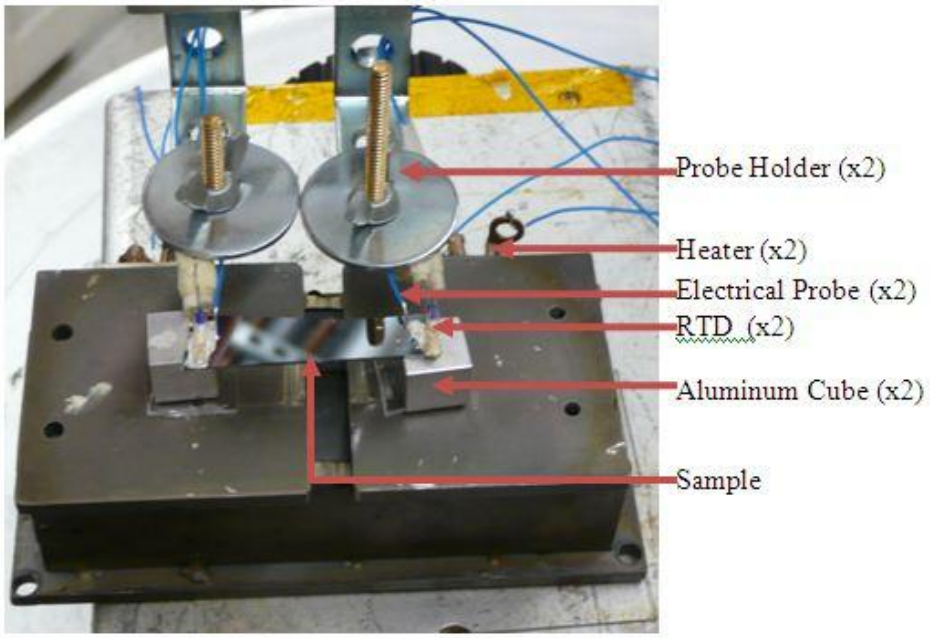

Figure 6 - Seebeck measurement device

In order to measure the temperature at each end of the film, two Omega F2010-100-B resistance temperature detectors (RTD) were used. These RTD's can measure temperature up to 600^{o}C and measure 2.0mm x 9.0mm x 0.8mm. RTD's were chosen over thermocouples in order to assure better contact with the film surface. The thermoelectric voltage was measured by placing a silver wire probe at each end of the film, equal distance apart from one another as the RTD's. The wire was placed parallel to the film surface to increase the surface area and again assuring good electrical contact. To both hold in place and enhance electrical and thermal contact, silver paste was placed between the detectors and the film.

All components of the device were placed under vacuum during testing, with the lead wires exiting through a sealed feed-through. The temperature and voltage values were measured using an Agilent Technologies 34970A data acquisition unit. This was then connected to a computer with a LabView based program which logged the temperatures and voltages and plotted the Seebeck coefficient versus temperature. The system was calibrated using both a Silicon and Germanium standard sample and compared with literature.

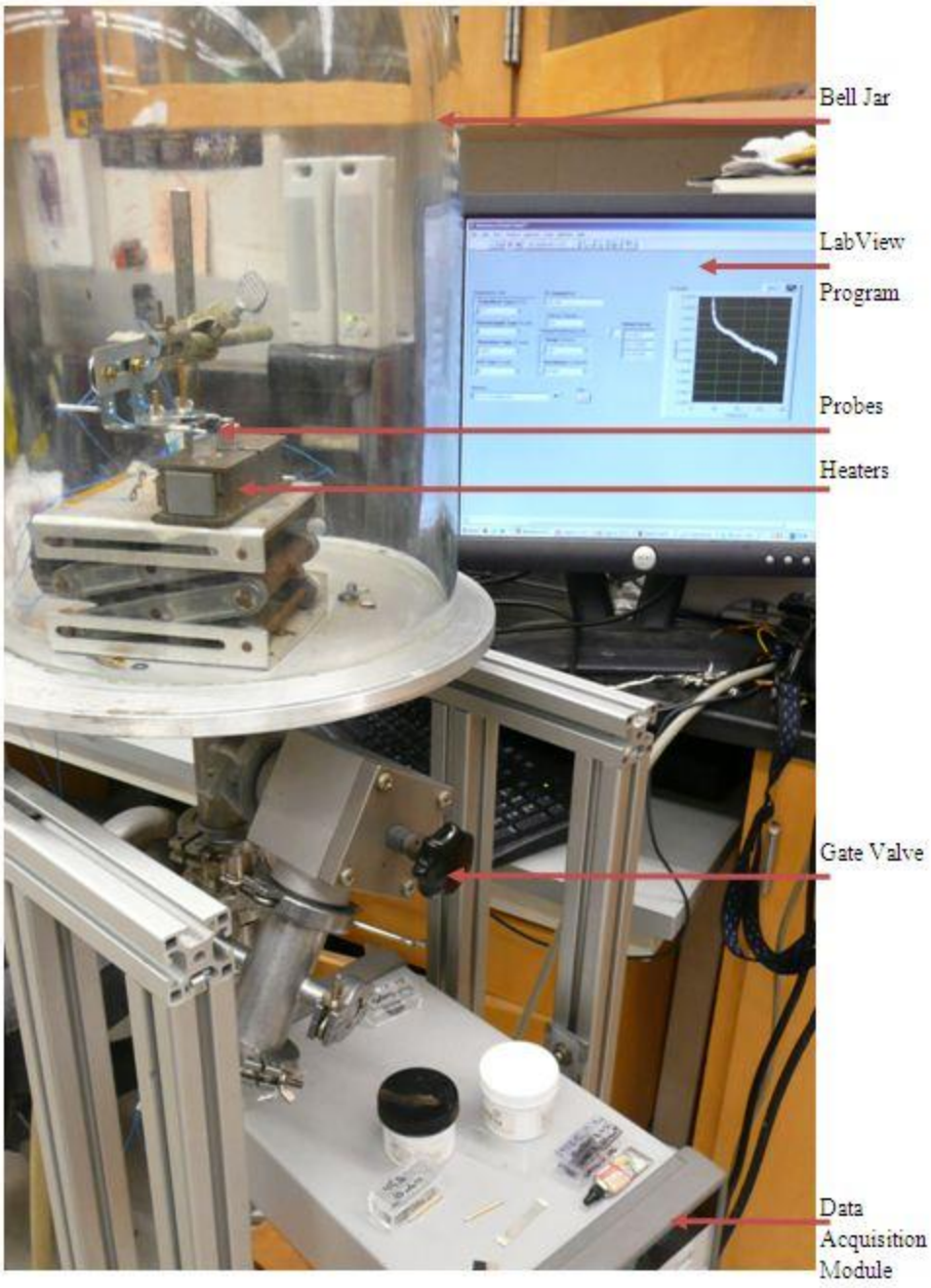

Figure 7 - Seebeck measurement device - Global view

2.3.4 Electrical Characterization

As a component of the figure of merit, zT, it is extremely important to measure the electrical conductivity of each sample. In addition, measuring the charge carrier type, concentration, and mobility will give increased insight into the deposited material. Such measurements are not possible from a simple electrical conductivity measurement such as a 4-point probe. To obtain this information, a Hall effect experiment can be conducted.

The Hall effect measurement utilizes an applied electric field which then sets in motion the charge carriers (holes or electrons) giving rise to a current, I. A magnetic field is imposed perpendicular to the direction of the charge flow resulting in a force brought upon the charge carriers causing them to deflect. The positive charge carriers (holes) will deflect in the opposite direction than the negative charge carriers (electrons) giving rise to the Hall voltage. In semiconductors, the simple Hall coefficient becomes slightly more complex due to the potential of both electrons and holes as charge carries, and in varying concentrations. When a moderate magnetic field is applied, the Hall coefficient can be described by

$$R_H = \frac{(-n\mu_e^2 + p\mu_h^2)}{e(n\mu_e + p\mu_h)^2} \qquad 2.3$$

where *n* is the electron concentration, *p* is the hole concentration, μ_e is the electron mobility , μ_h is the hole mobility and *e* the absolute value of the electronic charge [11].

NON-DOPED TITANIUM DIOXIDE GERMANIUM

3.1 Results and Discussion

3.1.1 Synthesis of TiO_2 – Ge

To determine the effect of Ge within the TiO_2 matrix the following samples were prepared. The RF deposition power and substrate temperature were maintained at 200W and 600^oC for all samples, respectively, as these parameters were determined to be optimum for Ge crystallization and TiO_2 rutile phase by Goyal et al.[9]. Deposition occurred for two hours with 30 minutes of pre-sputtering. Two targets were used to synthesize films at three pressures for each composition, yielding a total of six samples. Pressure, in a sputtering processes, has two affects (i) the total energy of the flux that eventually deposits on the substrate changes. Higher pressure induces more collisions and the sputtered flux loses its energy through a process called thermallization. (2) more ionizations in the plasma leading to higher sputtering rate.

The tabulated deposition parameters for each sample can be seen in the table below.

Sample Name	Composition (TiO_2:Ge)	Pressure (mTorr)
TiG1	30:70	5
TiG2	30:70	10
TiG3	30:70	15
TiG4	55:45	5
TiG5	55:45	10

TiG6	55:45	15

Table 1 – Deposition parameters of undoped samples

3.1.2 XRD Results

The figure below depicts the XRD of the samples prepared using the 70% Ge target and 45% Ge target. The anatase phase of TiO_2 is visibly present, along with the Ge cubic phase within the first three samples. At low pressure the TiO_2 seems to be of highest crystallinity, with higher pressures decreasing in crystallinity. Conversely, the Ge peaks develop more so as pressure is increased. The crystallite size of the Ge was calculated using Scherrer's formula, given by,

$$D = \frac{0.9\lambda}{\beta cos\theta} \qquad 3.1$$

The tabulated crystallite sizes can be seen in the table below, but it should be noted that Ge increased in size with increasing pressure for samples of both concentrations, with the exception of TiG1. In the case of TiG1 the signal from the XRD was very weak making it difficult to obtain consistent crystallite sizes. However, for the remaining TiO_2-Ge samples, the trend of increased crystallite size with increased pressure is reasonable. It is important to keep the Ge crystallite sizes below the phonon mean free path, which is 64 nm [14].

While the crystallinity of the Ge is seen in all samples, it appears that the TiO_2 is far less crystalline when deposited at higher pressures. The XRD for TiG4 through TiG6 demonstrates the decreasing crystallinity of TiO_2 while maintaining and

maybe even increasing the crystallinity of the Ge. This is very promising in terms of sufficiently growing a phonon-glass electron-crystal, as it is desirable to have the amorphous TiO_2 for decreased thermal conductivity, and crystalline Ge for enhanced electrical conductivity. However, while the Ge (111) peak intensified at 15mtorr and 45% Ge, the (220), and (311) peaks diminished greatly.

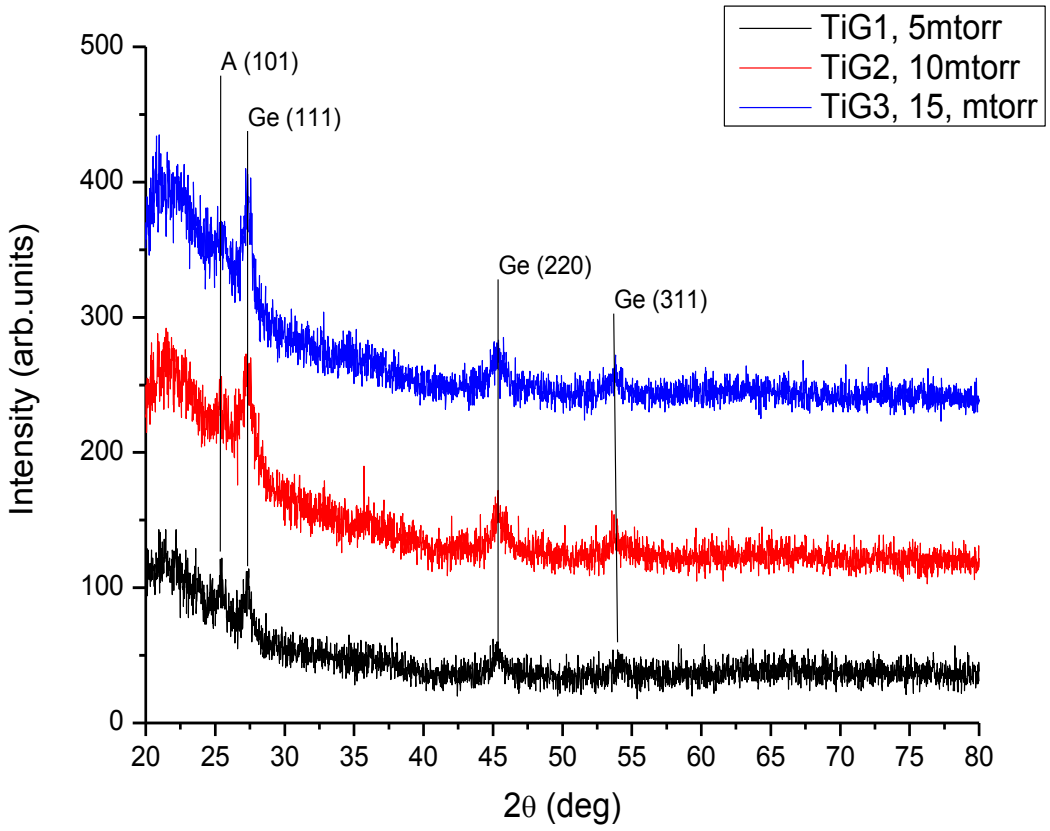

Figure 8 - XRD data for 70% Ge samples

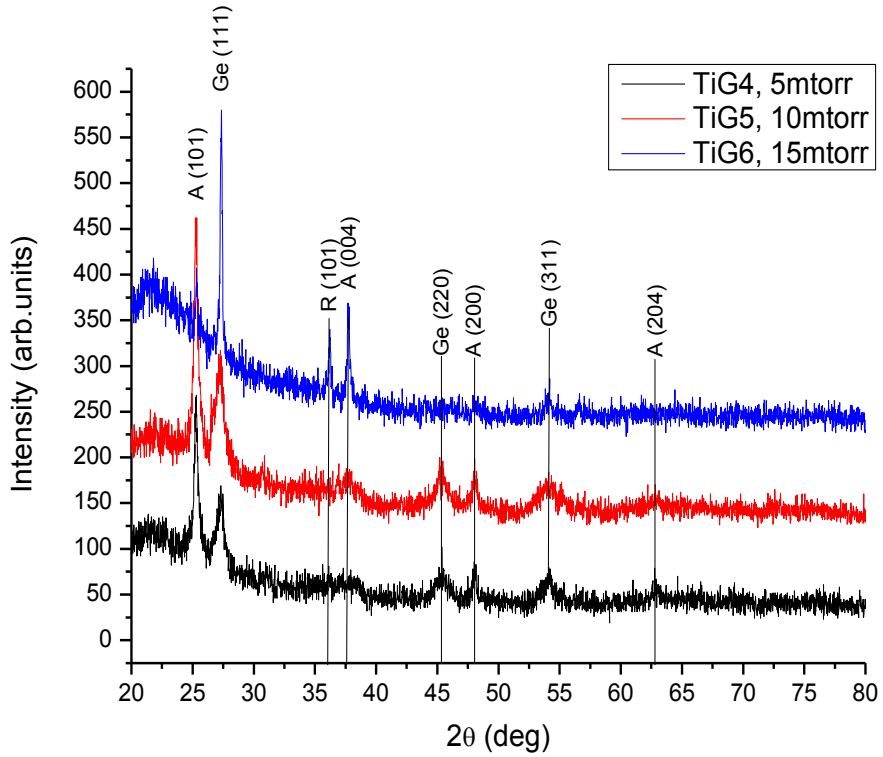

Figure 9 - XRD data for 45% Ge samples

Sample	TiG1	TiG2	TiG3	TiG4	TiG5	TiG6
Ge Crystal Size (nm)	11.9	9.3	11.8	9.9	9.7	46.6
"	12.3	9.9	13.1	11.2	12.1	37.2
"	13.1	8.2	11.4	12.2	11.3	36.8
"		11.1	13.1		12.0	29.6
Standard Deviation (nm)	0.61	1.21	0.88	1.15	1.11	6.97
Average (nm)	12.4333	9.625	12.35	11.1	11.275	37.55

Table 2 – Germanium crystallite sizes for undoped samples

3.1.3 SEM Results

Cross sectional SEM was carried out in order to obtain thickness measurements for each sample along with insight into the film growth at varying pressures and compositions. As seen in Figure 12 below, films deposited at higher pressures are visibly rougher. The increased gas collisions at higher pressures cause lower energy atoms with lower mobility to deposit on the substrate which leads to a rougher morphology. While it would be expected that the films with higher Ge concentration would be thicker, as Ge has a much higher sputtering rate, this is not the case. In order to rid the target of impurities it is pre-sputtered for some time before intended deposition. However, after several failed depositions of the 45% Ge target, it was determined that the target was becoming oxidized between depositions. To counter this, the pre-sputtering time was extended so as to remove the top layer of the target. During this process, even with a shutter covering the top of the substrate, some of the target material was most likely deposited. This reason leads to slightly thicker films, however helps decrease unwanted impurities deposited onto the majority of the film.

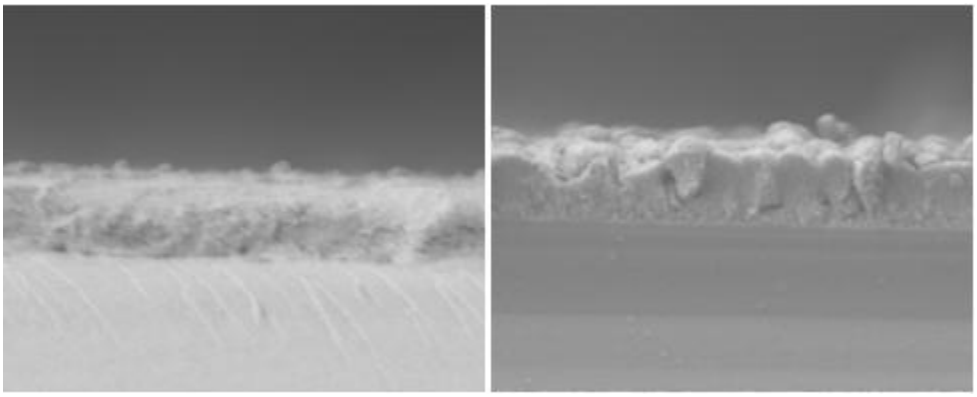

Figure 10 - Example of how increased deposition pressure increases film roughness. left; deposited at 5 mtorr. right; deposited at 15 mtorr

Sample	Thickness (nm)		Average
TiG1	520	493	506.5
TiG2	549	533	541
TiG3	685	678	681.5
TiG4	750	990	870
TiG5	1290	1193	1241.5
TiG6	1310	1313	1311.5
P3	715	708	711.5
P4	764	741	752.5
P5	890	905	897.5

Table 3 – Film thicknesses as measured by SEM for all samples

3.1.4 Electrical Conductivity Results

Electrical conductivities for the samples were measured using the van der Pauw method at room temperature. Each sample was prepared for measurement by soldering indium contacts onto the corners of each square sample. The table below shows the electrical conductivities of the prepared samples, except those for TiG2 and

TiG3. These two samples had become badly oxidized. Bulk TiO_2 has an electrical conductivity < 10^{-10} S/m [15]. After introducing both 45% and 70% Ge, the electrical conductivities of the films were significantly increased and approached that of bulk Ge. The conductivity for TiG1 has shown to be highest of the undoped samples, owing to the higher concentration of Ge within the target. Additionally, TiG4 exhibits the lowest of the conductivities, followed by TiG5 having the highest, and TiG6 dropping slightly. This fluctuation could be due to the crystallization of Ge at different pressures. The XRD results for TiG4 show the weakest Ge (111) peak intensity and the TiG6 sample with the strongest. While the TiG4, TiG5, and TiG6 samples all show relatively intense Ge (111) peaks, TiG5 also exhibits strong (220) and (311) Ge peaks. From this, it is reasonable to conclude that the increased electrical conductivity is due to the higher crystallinity of Ge within the TiG5 sample.

Sample	Electrical Conductivity (S/m)
TiG1	0.76
TiG2	-
TiG3	-
TiG4	0.16
TiG5	0.23
TiG6	0.20

Table 4 – Electrical conductivity for undoped samples

3.1.5 Seebeck Measurement Results

Seebeck measurements were carried out from room temperature to approximately 200^{o}C for each sample. To ensure for sufficient contact both thermally and electrically, high purity silver paste was applied between all interfaces of the probes

and film surface. By manually adjusting the variac heater controllers, a temperature gradient of between 10^{o}C and 20^{o}C was maintained across the film surface. The temperature was increased over a period of roughly 1 hour to ensure a smooth curve and to avoid compromising the temperature gradient. Additionally, the measurements were performed under a vacuum of at least 5mtorr. The vacuum system isolated the device from fluctuations that occur in ambient conditions.

The raw data for each Seebeck measurement were fit with a linear regression line, which was then plotted with relevant sample groups. Since the measurements were sometimes noisy, this allows for a better visualization of pertinent trends. All measurements on the undoped samples showed a positive trend as temperature was increased, however some samples initiated with a negative Seebeck voltage and progressively approached and entered positive voltages. This behavior is most noticeable in samples TiG3, TiG5, and TiG6. This transition can most likely be attributed to Ge within the TiO_2 matrix, as such behavior has been noticed in pure Ge [16]. The negative Seebeck voltage transitioning to a positive means that the film acts as an *n*-type material until a certain temperature, at which the dominating charge carrier switches, leading to the material acting as a *p*-type. The cause of such behavior has been attributed previously to low carrier concentration[17].

Of the 70% Ge samples, TiG3 has the largest slope, suggesting that at even greater temperatures the Seebeck coefficient could further exceed TiG1 and TiG2. The reason for this sample having a steeper slope may be due to a higher crystallinity of Ge, as seen in Fig. 10, combined with a small Ge crystallite size, allowing for a quantum confinement effect within the TiO_2 conduction band.

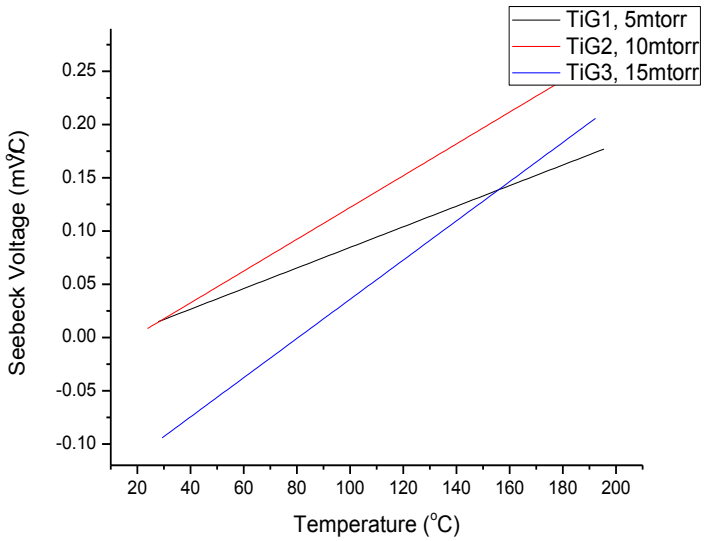

Figure 11 - Seebeck measurements for 70% Ge samples up to ~200 °C

The Seebeck measurements for the samples deposited from the 45% Ge target are shown in Figure 14 below. There is a significant increase in the Seebeck values of TiG4 as compared to the other two samples. TiG4, deposited at 5 mtorr, also exhibited the lowest electrical conductivity as described earlier, which does not intuitively correlate with this Seebeck value. Nonetheless, each sample follows a very similar trend in slope, which is encouraging for higher temperature performance. Additionally, all samples exceed the room temperature Seebeck coefficient of both room temperature and elevated temperature pure TiO_2 [21]. As seen in several papers in the literature, Seebeck coefficient significantly increase in magnitude at temperatures that reach and exceed 1000 °C [6][20][21]. As our setup was capable of reaching 200°C, the main focus was to establish a viable trend with which to move forward.

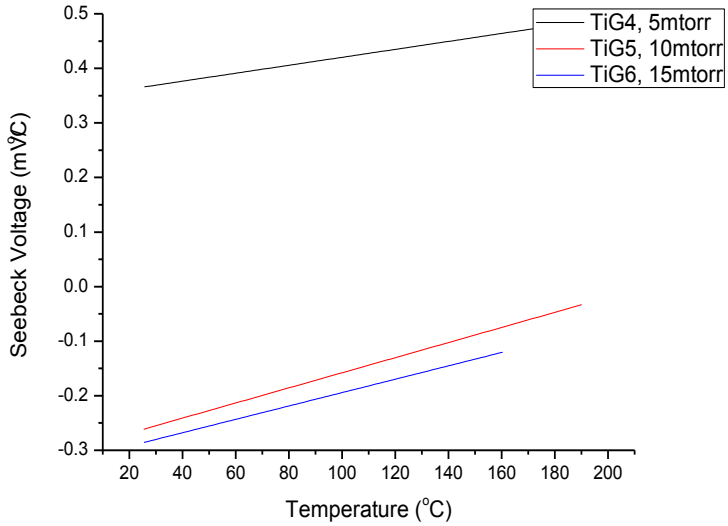

Figure 12 - Seebeck measurements for 45% Ge samples up to ~200 °C

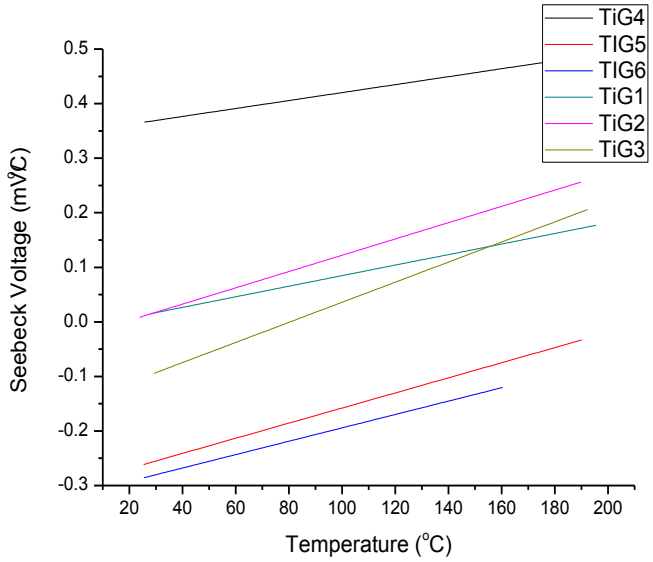

Figure 13 - Seebeck measurements for all undoped samples

ANTIMONY DOPED TRIALS

4.1 Results and Discussion

4.1.1 Synthesis of Sb doped TiO_2 – Ge

In efforts to increase the electrical conductivity of the prepared films while minimally disturbing the thermal conductivity of the TiO_2-Ge, an *n*-type dopant, such as Sb, is required. Antimony has been used with TiO_2 previously to aid with photocatalytic applications, and is explored in this study as a dopant [13][18]. Due to the limitation of times, samples were made at a single composition, while only varying the deposition pressure. This set of samples was prepared in a manner similar to the 45% Ge undoped samples, with the only difference being the introduction of 1% Sb. The RF deposition power and substrate temperature were maintained at 200W and ~600^{o}C for all samples, respectively. Deposition occurred for two hours with 30 minutes of pre-sputtering. Deposition pressures of 5 mtorr, 10 mtorr, and 15 mtorr were used. The tabulated deposition parameters for each sample can be seen in the table below.

Sample Name	Composition (TiO_2:Ge:Sb)	Pressure (mTorr)
P3	54:45:1	5
P4	54:45:1	10
P5	54:45:1	15

Table 5 – Deposition parameters for doped samples

4.1.2 XRD Results

The XRD results for each Sb doped sample can be seen below. Similarly to what was observed with the undoped 55% TiO_2 samples, increasing pressure shows a decrease of intensity for the anatase phase of TiO_2. Additionally, the Ge peaks seem strongest for the sample deposited at 10 mtorr. As stated earlier, it is ideal to create what is known as a phonon-glass electron crystal, as the TiO_2 becomes progressively lesser crystalline while Ge crystallinity increases.

The anatase phase that is seen in the 5 mtorr sample is no longer seen in the 10 mtorr and 15 mtorr samples. The decrease in TiO_2 crystallinity can be explained by the introduction of Sb into the TiO_2 lattice. As Sb forces itself into the TiO_2 lattice it distorts the lattice, leading to a progressively more amorphous phase. However, at the highest pressure of 15 mtorr, while still having amorphous TiO_2, it appears that the Ge too begins to lose crystallinity. This result is undesired as the Ge should remain crystalline, which is the case for the sample deposited at 10 mtorr.

As dopants are introduced, it has been observed that the TiO_2 becomes amorphous, which should have significant affects on the thermal conductivity on the film. While thermal conductivity measurements cannot presently be made due to the device still being assembled and tested, the amorphization of the TiO_2 should significantly decrease the thermal conductivity.

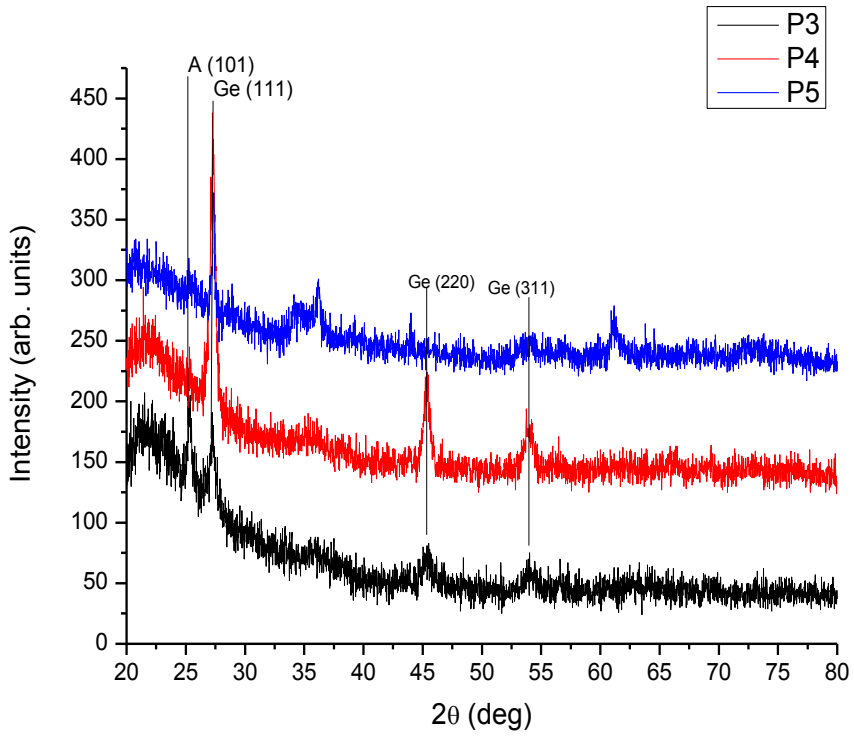

Figure 14 - XRd results for samples deposited at 5 mtorr, 10 mtorr, and 15 mtorr

Sample	P3	P4	P5
Ge crystallite size (nm)	11.7	15.5	31.2
"	11.5	15.3	21.3
"	10.2	15.9	24.4
"	10.2	18.5	24.9
"		152	25.7
Standard Deviation (nm)	0.81	1.38	3.60

Average (nm)	**10.9**	**16.08**	**25.5**

Table 6 – Ge crystallite sizes for doped samples

4.1.3 SEM Results

To obtain thickness measurements of each film, as well as to observe the formation of the film, cross sectional SEM was performed. As seen in Figure 17, the roughness of the film and the manner in which is grows changes with pressure. As the pressure increases a much more noticeable columnar structure appears, with a rougher surface. As seen in the image of the film deposited at lower pressure, a much smoother and finer structure has been grown.

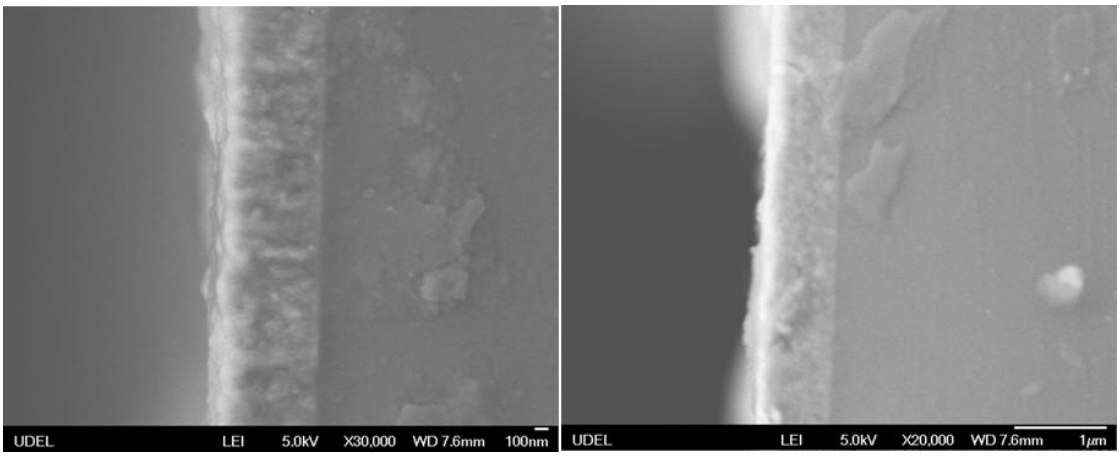

Figure 15 - left, sample deposited at 15 mtorr; right, sample deposited at 10 mtorr

Sample	Thickness (nm)	Thickness (nm)	Thickness (nm)	Average
P3	715	708	-	711.5

P4	764	741	769	752.5
P5	785	800	714	792.5

Table 6 – Film thicknesses for doped samples as measured by SEM

4.1.4 Electrical Conductivity Results

Initial electrical conductivity measurements have been carried out on each of the doped TiO_2-Ge samples at room temperature. The values are very similar to one another, with the conductivity minimally increasing with increasing pressure. As compared to the undoped 45% Ge films, the electrical conductivity has shown appreciable increase at all pressures, signifying that the Ge has maintained its crystallinity even with Sb doping.

Sample	Electrical Conductivity (S/m)
P3 (5 mTorr)	0.40
P4 (10 mTorr)	0.53
P5 (15 mTorr)	0.64

Table 7 – Electrical conductivity of doped samples

4.1.5 Seebeck Measurement Results

Seebeck measurements were performed on each of the doped samples up to temperatures of roughly 200 ^{o}C. All measurement parameters were the same as those for the undoped samples. Similarly to some of the undoped samples, the Sb doped films have Seebeck measurements originating with a negative voltage and increasing with temperature. The 15 mtorr sample exhibits a very strong upward trend over the first 200 ^{o}C, most likely because the Sb and Ge are active within the sample TiO_2 matrix. However, the Ge in the 15 mtorr sample was not as crystalline as the 10 mtorr sample, yet performed better. This could be due to higher oxidation in the P4 sample at the time of measurement. When comparing all samples, the Sb doped films did not perform significantly different than the undoped, which was unexpected. However, as mentioned before, and seen in literature, increased temperature will play a significant role in increasing the Seebeck values [20].

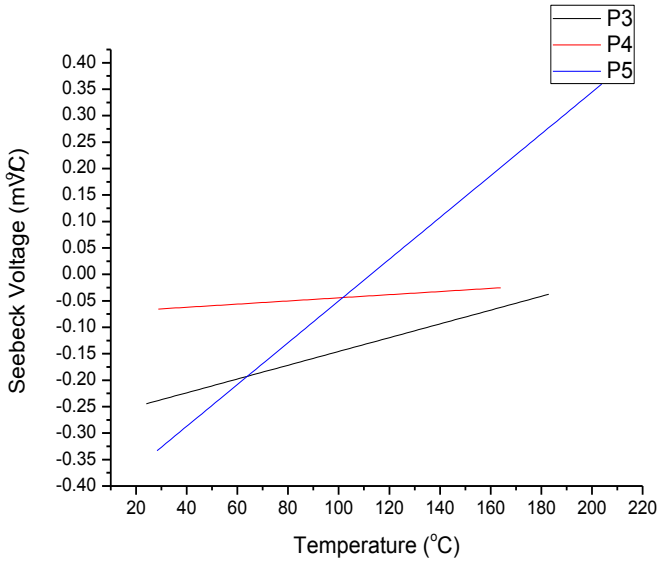

Figure 16 - Linear fit lines for Seebeck measurements of Sb doped samples

CONCLUSION

Over the course of this research, a slow progression can be seen in regards to increasing the performance of TiO_2-Ge as a thermoelectric material. While several crucial measurements must still be made before a definitive conclusion can be made, this research will be able to provide valuable insight for future work. The initial testing with only TiO_2-Ge made the idea of creating a phonon-glass electron crystal more reasonable. It was demonstrated that as the pressure is increased it was possible to attain both amorphous TiO_2 and crystalline Ge. While this was seen with XRD, the electrical conductivity also confirmed that the Ge was increasing the electrical conductivity. However, it remains to be seen whether the figure of merit, zT, is increased since the bulk thermal conductivity of Ge is very high compared to TiO_2. The doped samples showed slightly increased electrical conductivity as compared to the undoped. Even while minimal, this is encouraging for future work, as the concentration of Sb and Ge can be manipulated so as to become optimized.

Additionally, while the Seebeck measurements provided initial insight into the behavior of the nanocomposite, measurements at higher temperatures must be pursued. Since the waste heat of many systems is at very high temperatures, it is crucial to understand the performance of this material at equally high temperatures. However, with the data that is currently available, a trend of increasing Seebeck with increasing temperature is seen, which is very encouraging for the future of this material.

Overall, Sb doped TiO_2-Ge shows promise for use as a thermoelectric material. Samples reported electrical conductivities significantly higher than bulk TiO_2, and XRD results showed amorphous TiO_2, which gives confidence that the thermal conductivity of the samples should be minimally affected by the Ge and Sb. With these considerations, the zT value should be respectable.

In conclusion, with the United States alone consuming 604.4 million gallons of petroleum, and 378 million gallons of motor gasoline each and every day, it is imperative that new methods of energy recycling, harvesting and production are found [19]. Thermoelectrics offers a method to recoup energy lost as heat and convert it into useful electricity, therefore increasing the efficiency of a particular device. While many continue to search for completely new forms of energy, the importance of trying to better those which society already has must not be overlooked. With increased energy efficient devices will come both a cleaner world to live in and a more economically stable market.

Works Cited

[1]. Cushing, OK WTI Spot Price FOB (Dollars per Barrel). *Petroleum Navigator.* [Online] March 3, 2010. http://tonto.eia.doe.gov/dnav/pet/hist/LeafHandler.ashx?n=PET&s=rwtc&f=d.

[2]. The Z-Max Performance Advantage. [Online] 2009. http://www.tellurex.com/pdf/tellurex-capabilities.pdf.

[3]. Advanced Technologies and Energy Efficiency. *United States Department of Energy, Energy Efficiency and Renewable Energy.* [Online] 2010. http://www.fueleconomy.gov/feg/atv.shtml.

[4]. Johnson, C. *Physics In an Automotive Engine.* Chicago, IL : s.n., 2003.

[5]. Tellurex. The Most Frequently Asked Questions About Thermoelectric Power Generation Technology. *Tellurex Corporation.* 2006. www.tellurex.com.

[6]. G. J. Snyder, Complex thermoelectric materials. *Nature*. 7, 105-113 (2008)

[7]. **Callister, William D.** The Hall Effect. *Materials Science and Engineering an Introduction.* York : Wiley, 2007.

[8]. **Callister, William.** *Materials Science and Engineering An Introduction.* New York : Wiley, 2007, pg 672.

[9]. Sputtering Targets. *TYR.* [Online] Huizohou Tian Yi Rare Materials Company. http://www.rare-metal.com/en/bigclassmemo.aspx?id=40.

[10]. The Scherrer Formula for X-Ray Particle Size Determination". Phys. Rev. 56 (10): 978–982 (1939)

[11]. S. O. Kasap, Hall Effect in Semiconductors. *Web-Materials*. 1, 1-8 (2001)

[12]. A. Goyal, TiO2-Ge Nanocomposites for Photovoltaic Applications. ProQuest (2006).

[13]. J. Moon, Preparation and characterization of the Sb-doped TiO2 photocatalysts. *J. of Mat. Sci.* **36**, 949-955, (2001)

[14]. **Wolf, Helmut.** *Semiconductors,* Wiley Pubilcations, 1971.

[15]. Titanium Dioxide - Titania. *AZO Materials.* Jan 11, 2002. [Cited: Apr 13, 2010.] http://www.azom.com/details.asp?articleid=1179.

[16]. E. Balikci, R. Abbaschian. The Seebeck coefficient of the solid and liquid germanium. *J. of Mat. Sci*, **40** 1475-1479, (2005)

[17]. C.A. Domenicali, J. Appld. Phys., **28,** 749, (1969)

[18]. S. V. Eremeev, Effects of Antimony Doping on Electronic Structure. *Russian Physics*, Vol. 47, No. 7, 2004.

[19]. Petroleum Statistics. *U.S. Energy Information Administration.* [Online] Jan 26, 2010. http://tonto.eia.doe.gov/energyexplained/index.cfm?page=oil_home#tab2.

[20]. K. Park, K.Y. Ko *Effect of TiO_2 on high-temperature thermoelectric properties of* ZnOJournal of Alloys and Compounds **430** 200–204 (2007)

[21]. D. Mardare, A. I. Cuza. *The Seebeck Coefficient of TiO_2 Thin Films.* Journal of Optoelectronics and Advanced Materials 7-2. 721 – 725 (2005)